nature communications

Article

https://doi.org/10.1038/s41467-025-56534-1

Transient pulsed discharge preparation of graphene aerogel supports asymmetric Cu cluster catalysts promote CO_2 electroreduction

Received: 7 March 2024

Accepted: 17 January 2025

Published online: 31 January 2025

Check for updates

Kaiyuan Liu[1,2], Hao Shen[3], Zhiyi Sun[4], Qiang Zhou[5], Guoqiang Liu[6], Zhongti Sun[3], Wenxing Chen[4], Xin Gao[1] & Pengwan Chen[1,2,7]

Designing asymmetrical structures is an effective strategy to optimize metallic catalysts for electrochemical carbon dioxide reduction reactions. Herein, we demonstrate a transient pulsed discharge method for instantaneously constructing graphene-aerogel supports asymmetric copper nanocluster catalysts. This process induces the convergence of copper atoms decomposed by copper chloride onto graphene originating from the intense current pulse and high temperature. The catalysts exhibit asymmetrical atomic and electronic structures due to lattice distortion and oxygen doping of copper clusters. In carbon dioxide reduction reaction, the selectivity and activity for ethanol production are enhanced by the asymmetric structure and abundance of active sites on catalysts, achieving a Faradaic efficiency of 75.3% for ethanol and 90.5% for multicarbon products at −1.1 V vs. reversible hydrogen electrode. Moreover, the strong interactions between copper nanoclusters and graphene-aerogel support confer notable long-term stability. We elucidate the key reaction intermediates and mechanisms on Cu_4O-Cu/C_2O_1 moieties through in situ testing and density functional theory calculations. This study provides an innovative approach to balancing activity and stability in asymmetric-structure catalysts for energy conversion.

The electrochemical catalytic carbon dioxide reduction reaction (CO_2RR) driven by renewable electricity provides a green solution for energy and environmental crises[1,2]. Multi-carbon compounds (C_{2+}), such as ethylene, ethanol, and propanol, have higher accessional value compared to single-carbon organic products (C_1)[3,4]. Among them, ethanol (EtOH) is considered an outstanding liquid fuel and industrial chemical owing to its significant energy density and wide range of applications[3,5,6]. Besides, EtOH also possesses the advantages of long-term storage, ease of transportation, and scalability[7,8]. Due to the high energy barrier associated with C-C bond formation, it competes with the formation of C-H or C-O bonds, making it challenging to generate C_{2+} liquid products through CO_2RR. Recently, multiple investigations have demonstrated that copper-based catalysts feature a highly efficient conversion from carbon dioxide to C_{2+} products, with high

[1]School of Mechatronical Engineering, Beijing Institute of Technology, Beijing 100081, China. [2]Yangtze Delta Region Academy of Beijing Institute of Technology, Jiaxing, Zhejiang 314019, China. [3]School of Materials Science and Engineering, Jiangsu University, Zhenjiang, Jiangsu 212013, China. [4]Energy & Catalysis Center, School of Materials Science and Engineering, Beijing Institute of Technology, Beijing 100081, China. [5]China Academy of Ordnance Science, Beijing 100089, China. [6]School of Materials Science and Engineering, Anhui University of Technology, Ma-An-Shan, Anhui 243002, China. [7]School of Materials Science and Engineering, Beijing Institute of Technology, Beijing 100081, China. e-mail: ztsun@ujs.edu.cn; wxchen@bit.edu.cn; gaoxin@bit.edu.cn; pwchen@bit.edu.cn

selectivity[9–11]. Even when the C-C coupling process is successfully achieved on copper catalysts, the production of other complex C_{2+} products, such as ethylene and acetate, remains a significant challenge. Therefore, achieving control over the evolution of reaction intermediates while designing highly active catalysts is crucial for advancing efficient electrochemical CO_2RR to produce ethanol. To overcome this obstacle, the catalyst must possess unique electronic and structural properties that facilitate the selective formation of ethanol. Specifically, the catalyst should provide a favorable reaction environment that stabilizes key intermediates involved in the CO_2 reduction pathway to ethanol. Modulating the local electronic structure of catalyst active sites to enhance the binding affinity for specific reaction intermediates can effectively steer the reaction towards ethanol rather than other byproducts. Concurrently, the catalyst must maintain a high density of active sites to facilitate the selective reduction of CO_2 to ethanol. In a word, the catalyst should allow for effective electronic interactions with CO_2 and its intermediates, promoting the desired reaction pathway while inhibiting competing processes. Customizing asymmetric nanostructured catalysts represents a promising solution in this context. This approach involves precise regulation of the geometric structure, morphology, coordinate structure, and size of catalysts, thereby optimizing specific surface area, and the types and quantities of specific active sites, ultimately leading to improved catalytic ability[12–15]. Additionally, doping with other elements, whether metals or non-metals, can introduce new active sites, modify electronic properties, and enhance stability[16–19]. Regulating the interface binding between metals and carriers is another critical strategy that can strengthen metal-support interactions, improve dispersion of catalytic species, and enhance overall catalyst durability and performance[20–22]. The construction of atomically dispersed active sites represents a cutting-edge approach, offering maximal atomic efficiency and unique coordination environments that can dramatically increase catalytic activity and selectivity[23–26]. Collectively, these strategies provide the multifaceted approaches available for advancing the development of high-performance catalysts. However, the selectivity and current density for electrocatalytic CO_2 reduction to C_{2+} products also remain inadequate[4,27–29].

Atomically dispersed catalysts with asymmetric structures generate localized polarization fields due to charge density gradients, making them highly suitable for the electrocatalytic CO_2RR by polarizing nonpolar CO_2 molecules[30–33]. However, these catalysts often face challenges related to long-term stability. Carbon-supported catalysts containing metal or metal oxide nanoclusters offer a high density of active sites for electrocatalytic reactions and feature precisely tunable metal-support architectures[34–37]. This tunability facilitates the design of catalysts with both high selectivity and enhanced long-term stability for CO_2RR[38–40]. Specifically, the active copper atoms within nanostructured Cu or CuO_x clusters on carbon supports exhibit favorable adsorption properties for intermediates such as *CO and *H, leading to high selectivity for C_{2+} products and ethanol[41–44]. By adjusting the carbon-supported copper nanocluster configuration, it is possible to construct high-density asymmetric active centers that efficiently convert CO_2 to ethanol during CO_2RR. This design strategy may address the limitations of poor ethanol selectivity and insufficient long-term stability in electrocatalytic CO_2RR. The pulsed discharge method is capable of delivering high-density current through conductive carbon-based supports within microseconds, generating instantaneous intense electric effect and heat effect that induce precursor metal salts to undergo micro-explosions induced from rapid decomposition and sublimation. The ultra-short duration of the pulsed discharge leads to a rapid temperature drop, creating a quenching effect that is conducive to the formation of uniform metal nanoclusters. Consequently, this method is well-suited for synthesizing size- and morphology-controlled metal nanoclusters with asymmetric structure on conductive carbon-based supports. Leveraging the rapid non-equilibrium strategy to synthesize structurally tunable nanocluster/graphene catalysts exhibits extraordinary potential for applications in the electrocatalytic CO_2RR. The multi-step reaction process of CO_2 reduction to ethanol is characterized by high energy barriers and intricate mechanisms[45–48]. Synthesis of nanocluster catalysts with well-defined active centers using the pulsed discharge method facilitates the study of the electrocatalytic CO_2RR mechanisms on asymmetric active sites and provides deeper insights into the structure-activity relationships in electrochemical catalysis.

In this work, graphene aerogels support Cu nanocluster catalysts (Cu Clu/GAs) with Cu_4O-CuC_2O_1 atomic interaction structures are prepared by a pulsed discharge strategy efficiently. The size of nano coppers on GA can be modulated from 1.4 nm to 7.5 nm by pulsed discharge conditions. Impressively, the Cu Clu/GAs exhibit high selectivity and activity in CO_2RR to produce EtOH. Moreover, this catalyst proposes a long-term stability (> 60 h). The Cu Clu/GAs with asymmetric distribution of atomic and electronic coordination structures are confirmed through atomic-level structural analysis. In situ X-ray absorption fine structure (XAFS) measurements for $Cu_{1.7}$ Clu/GAs demonstrate that the asymmetric Cu_4O-CuC_2O_1 moieties could promote the EtOH production in the electrocatalytic CO_2RR process. The oxide state of Cu in $Cu_{1.7}$ Clu/GAs is decreased through the detection of in situ XAFS and in situ near-ambient pressure X-ray photoelectron spectroscopy (NAP-XPS) during the CO_2RR process. The main intermediates are detected by in situ attenuated total reflectance Fourier transform infrared spectroscopy (ATR-FITR) and in situ Raman tests. The pathways of CO_2RR on Cu_4O-CuC_2O_1 are figured out by the calculation of density functional theory (DFT). Additionally, other metal clusters supported by GAs (M Clu/GAs, M = Co, Ni, Pt, Ru) with asymmetric structures could be synthesized by pulsed discharge approach.

Results and discussion

Synthesis and morphology characterizations of Cu Clu/Gas

Graphene hydrogel (GH) could be prepared by the hydrothermal assembly method[49]. The graphene oxide solvent was poured into a glass bottle with an inner diameter of 15 mm and a depth of 25 mm. The copper chloride was added to the suspension to form a certain concentration of $CuCl_2$ solvent. The GH was immersed in the $CuCl_2$ solvent for 5 h. Then the beaker including GH and solvent were frozen using liquid nitrogen. During the frozen vacuum drying process, the ice sublimated and the $CuCl_2$ nano-crystals were separated on the surface of graphene aerogel (GA, Supplementary Fig. 1). Then the GA in size of $\Phi 9 \times 15$ mm was fabricated (with $CuCl_2$ 5 wt%). The content of $CuCl_2$ can be modified by the mass of $CuCl_2$ in the bottle. The $CuCl_2$/GAs were compressed into the copper tube by copper plugs (Supplementary Video 1). Subsequently, the tube was fixed with two electrodes for discharge (Supplementary Figs. 2 and 3). After the charging of the capacitor, the air switch was triggered for pulsed discharge. The $CuCl_2$ would be decomposed into Cu and chlorine (Cl_2) rapidly in the discharge tube due to the transient Joule heating. After pulsed discharge, the decomposed Cu atoms converged to form Cu clusters on the GAs during a rapid cooling process to form Cu Clu/GA specimens. Figure 1a presents the formation schematic diagram of Cu Clu/GA.

A presentative discharge current waveform in the copper discharge tube containing a $CuCl_2$/GA is shown in Fig. 1b, revealing the typical current-voltage (I-U) waveforms in the resistance-inductance-capacitance (RLC, Supplementary Fig. 4) circuit during the pulsed discharge. Our pulsed discharge technique shares similarities with the spark plasma sintering (SPS) technology, wherein self-heating via Joule heating and localized plasma synergistically facilitate the decomposition-diffusion-agglomeration process, leading to the formation of dispersive metal nanoclusters from metal salt nanocrystals. The difference lies in the SPS using an on-off DC pulsed current, whereas the pulsed discharge employs a current pulse of underdamped waveform with a duration of several hundred microseconds. When the 3D

https://doi.org/10.1038/s41467-025-56534-1

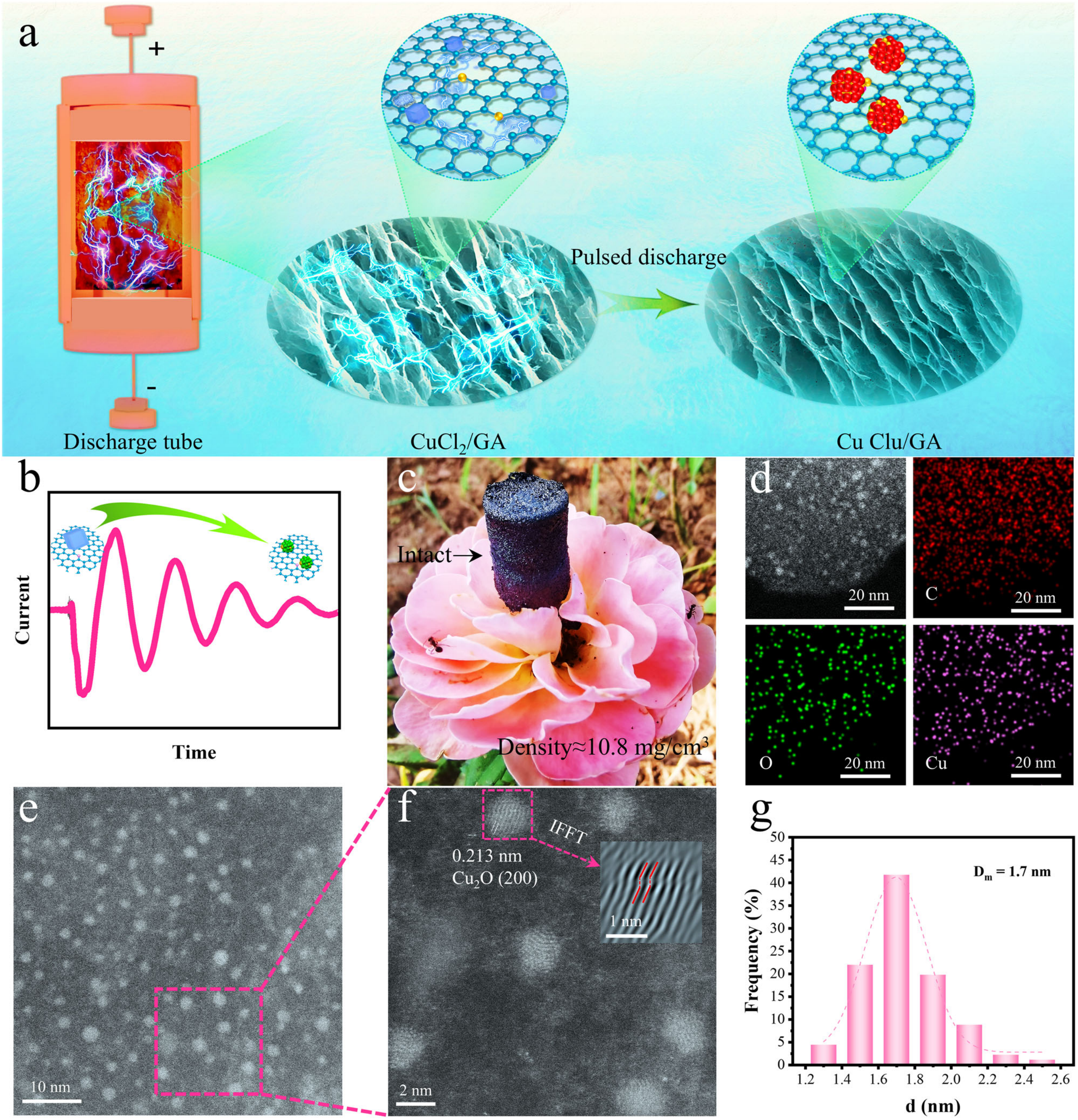

Fig. 1 | The synthesis and characterizations of $Cu_{1.7}$ Clu/GAs. a A schematic plot of the preparation strategy by the transient pulsed discharge. **b** The current curve of the circuit in the $Cu_{1.7}$ Clu/GAs synthesis process. **c** A photomacrograph of $Cu_{1.7}$ Clu/GAs. **d** EDS mapping images, C (red), O (green), and Cu (purple). **e** A HAADF-STEM figure (dark field). **f** The local magnified image of $Cu_{1.7}$ Clu/GAs. Inset is a locally enlarged IFFT image of a marked single cluster. **g** Nanoclusters size distribution frequency.

porous GA with capacitive properties is applied by the current pulse with an underdamped waveform, its equivalent resistance is significantly lower than that under direct current. The GA within the copper tube can obtain sufficient current, leading to the generation of Joule heating effects by itself (Supplementary Fig. 5 and Note 1, Supplementary Video 2). GA supports loaded metal nanocluster catalysts that could be rapidly synthesized under the transient pulsed discharge technology. Especially, the I-U curves (Supplementary Fig. 6) indicate that the resistance of the circuit did not change during the pulsed discharge process, implying that the GA support was no decomposition and phase change after the transient pulsed discharge treatment, as evidenced in the recovered intact GA after pulsed discharge (Fig. 1c). The $CuCl_2$ nanocrystals in GA decomposed to form Cu^{2+} and Cl^- ions under the action of high temperature. These ions burst out and agglomerate to form clusters anchoring on the GA support during pulsed discharge. Moreover, the air in the porous and defects of GA may form multiple local corona discharge plasma, consisting of O ions and N ions. This effect could potentially activate the metal clusters, causing them to repeatedly vaporize and condense on the graphene, resulting in uniformly sized nanoscale metal clusters and establishing strong atomic interactions with the GA support.

Additionally, the high-frequency varying current on the copper tube generates a circular time-varying electromagnetic field inside the copper tube. After the decomposition of the metal salt nanocrystals loaded on the graphene aerogel, the resulting Cu ions move under the influence of the changing electric and magnetic fields, which accelerates the diffusion process of the metal atoms and may result in a more uniform distribution of the nanoclusters. The magnetic pinch effect caused by the dynamic electromagnetic field inhibits the radial expansion of the formed ions[50], which maintain a relatively high-density plasma including Cu, and O ions in GA. Consequently, the mixed Cu and O ions agglomerate to form clusters on the defects of graphene (Supplementary Figs. 7 and 8). Cu clusters/nanoparticles of various sizes (1.4 nm, 1.7 nm, 2.7 nm, 4.1 nm, and 7.5 nm) with the same amount of Cu loading were synthesized and securely anchored onto graphene by adjusting the charging voltage to increase the pulsed discharge duration. They are identified as $Cu_{1.4}$ Clu/GAs, $Cu_{1.7}$ Clu/GAs, $Cu_{2.7}$ NPs/GAs, $Cu_{4.1}$ NPs/GAs, and $Cu_{7.5}$ NPs/GAs, respectively (Supplementary Figs. 9–14). The results in Supplementary Table 1 indicate that inputting higher energy in a shorter time would result in the formation of smaller Cu nanoparticles on GAs.

The density of $Cu_{1.7}$ Clu/GA was calculated at ~10.8 mg/cm^3 through precise testing, which is very lightweight compared to dense materials (Supplementary Table 2). The 3D porous structure of $Cu_{1.7}$ Clu/GA is also performed by scanning electron microscope (SEM, Supplementary Fig. 10). There is no significant difference in the low magnification transmission electron microscopy (TEM) image between $Cu_{1.7}$ Clu/GA and the initial GA. A lot of nanoclusters are distributed on graphene by the high-magnification TEM images. Figure 1d shows the mapping energy dispersive spectrum of $Cu_{1.7}$ Clu/GAs, where the carbon (C), oxygen (O), and Cu elements are uniformly distributed in the reduced graphene oxide (r-GO). The Cu atoms content of $Cu_{1.7}$ Clu/GA is 8.41 wt % measured by inductively coupled plasma optical emission spectrometry (ICP-OES). Figure 1e presents a high-angle annular dark-field scanning transmission electron microscopy (HAADF-STEM) image of $Cu_{1.7}$ Clu/GAs, plenty of clusters were dispersed onto the graphene. Uniformly sized Cu clusters were so evenly seeded on graphene because the instantaneous characteristics of pulsed discharge inhibit the continued growth of these Cu clusters. Figure 1f shows the higher magnification HAADF-STEM image of $Cu_{1.7}$ Clu/GAs, and some local crystal plane spacing could be measured, while the Cu_2O crystal features were identified. The inset is a locally enlarged inverse fast Fourier transform (IFFT) image of a marked single cluster. Nanoclusters exhibit severe lattice distortion, which is due to the thermal effect and electromigration coupling effect generated by high-frequency pulsed discharge, resulting in atomic diffusion at different speeds in different directions (Supplementary Fig. 15). Meanwhile, Cu nanoclusters are highly susceptible to oxidation due to their high specific surface energy. Subsequently, a wide range of Cu nanoclusters with different batches (Supplementary Fig. 11) were counted by the Nanomeasure software, and the distribution of frequency-diameter was shown in Fig. 1g. It can be seen that Cu clusters with a diameter of 1.7 nm predominate (> 40%), with over 85% of the clusters distributed within the 1.5–2.0 nm range.

Electrocatalytic characterizations

The electrocatalytic CO_2RR performance of $Cu_{1.4}$ Clu/GAs, $Cu_{1.7}$ Clu/GAs, $Cu_{2.7}$ NP/GAs, $Cu_{4.1}$ NP/GAs, and $Cu_{7.5}$ NP/GAs was evaluated by an H-type cell (Supplementary Fig. 16). Linear sweep voltammetry (LSV) plots (Fig. 2a) are employed to acquire polarisation curves in the CO_2-saturated 0.5 M $KHCO_3$ aqueous solution. Moreover, the activity of $Cu_{1.7}$ Clu/GAs exhibited the lowest onset potential and the fastest decreasing current density in all samples. The FEs of EtOH (FEs_{EtOH}) were obtained at different potentials (from −0.8 V to −1.2 V) for $Cu_{1.7}$ Clu/GAs and $Cu_{7.5}$ NP/GAs, as shown in Fig. 2b. Impressively, the FE_{EtOH} of $Cu_{1.7}$ Clu/GAs reached 75.3% at −1.1 V, while the FEs_{EtOH} of other samples (Supplementary Fig. 17) remained at the relatively lower level in the wide potential range. Furthermore, the FEs_{EtOH} of $Cu_{1.7}$ Clu/GAs could be maintained > 55% at −0.9 V to −1.2 V, exhibiting high selectivity on EtOH production from CO_2RR, which was better than the performances of $Cu_{2.7}$ NPs/GAs, $Cu_{4.1}$ NPs/GAs, and $Cu_{7.5}$ NPs/GAs. Moreover, the partial current densities of EtOH (J_{EtOH}) of $Cu_{1.7}$ Clu/GAs were calculated (Fig. 2c) from −0.8 V to −1.2 V, and the optimal J_{EtOH} was −33.5 mA cm^{-2} at −1.1 V. The current densities of other samples were weaker than that of $Cu_{1.7}$ Clu/GAs at the potential range. Impressively, the performance of $Cu_{1.7}$ Clu/GAs exceeded the most listed electrochemical catalysts on CO_2RR-to-EtOH in recent literature (Supplementary Fig. 18 and Supplementary Table 3). Figure 2d provides the FEs of various products on $Cu_{1.7}$ Clu/GAs at the operated potential from −0.6 V to −1.2 V vs. RHE. The main products were H_2 and CO at the higher potentials (−0.6 V and −0.7 V), and the product of EtOH was first detected when the potential decreased to −0.8 V (Supplementary Table 4), EtOH dominated at lower potentials (from −0.9 V to −1.2 V). Meanwhile, the FEs of C_1, and C_{2+}, H_2, were counted and presented in Supplementary Fig. 19, and FE_{C2+} reached a surprising 90.5%. Additionally, the CO_2RR performance of $Cu_{1.4}$ Clu/GAs at different potentials was provided in Supplementary Fig. 17 and Supplementary Table 5, the FE_{EtOH} reached a decent 66.5% at −0.9 V.

The electrochemical surface area (ECSA) is employed to further investigate the performance of catalysts, which provides a qualitative assessment of the density of active sites and specific surface area. The double-layer capacitance method was used to calculate the ECSA values for $Cu_{1.4}$ Clu/GAs and $Cu_{1.7}$ Clu/GAs, with the results presented in Supplementary Fig. 20. The ECSA values for $Cu_{1.4}$ Clu/GAs and $Cu_{1.7}$ Clu/GAs reached 116.5 and 108.8 m^2 g^{-1}, respectively. The ECSA value of our catalysts exceeds that of the most recently reported catalysts (Supplementary Table 6), indicating that the active site density and specific surface area of $Cu_{1.7}$ Clu/GAs and $Cu_{1.4}$ Clu/GAs are at a relatively high level among similar catalysts. Interestingly, the ECSA value of $Cu_{1.7}$ Clu/GAs is slightly higher than that of $Cu_{1.4}$ Clu/GAs, suggesting that the more oxidized 1.4 nm Cu atoms do not provide a greater number of active sites compared to the less oxidized 1.7 nm Cu atoms. This result is consistent with the results obtained from the electrochemical performance tests for CO_2 reduction reactions.

The long-term stability of CO_2RR is crucial and the potential issue of metal dissolution should not be overlooked. The stability measurement results of $Cu_{1.7}$ Clu/GAs are shown in Fig. 2e, the FE_{EtOH} of $Cu_{1.7}$ Clu/GAs keep on > 74% with a negligible current density loss at the operated potential of −1.1 V during the 60 h stability measurement. At the same time, all the J_{EtOH} remain below −33.0 mA cm^{-2} from beginning to end. These indicate that $Cu_{1.7}$ Clu/GAs possess long term stability in the electrocatalytic CO_2RR process. The comprehensive performance of $Cu_{1.7}$ Clu/GAs is evaluated in the electrochemical catalytic CO_2RR process, as shown in Fig. 2f. Compared to Cu/$N_{0.14}$C[34] and $Cu_{1.4}$ Clu/GAs, the $Cu_{1.7}$ Clu/GAs is the most versatile in all aspects. The long-term stability of $Cu_{1.4}$ Clu/GAs is not as robust as that of $Cu_{1.7}$ Clu/GAs, maintaining stability for only 25 hours at −0.9 V vs. RHE without significant degradation. Furthermore, the CO_2RR performance of $Cu_{1.7}$ Clu/GAs in a flow cell (Fig. 2g) was conducted, and the LSV curve of $Cu_{1.7}$ Clu/GAs is presented in Fig. 2h. The FE_{EtOH} and J_{EtOH} reached 68.7% (Fig. 2i) and −339.8 mA cm^{-2} (Fig. 2j) at −1.1 V vs. RHE respectively, which were competitive compared to previous report (Supplementary Table 3). As the potential decreases from −0.6 V to −1.2 V vs. RHE, EtOH and C_{2+} products come to dominate, suppressing the production of C_1 products and H_2. Furthermore, the stability measurement (60 h) manifested that the loss of potential and FE_{EtOH} were ignorable at −500 mA cm^{-2} for $Cu_{1.7}$ Clu/GAs in the flow cell (Fig. 2k). The impressive activity, selectivity, and stability of $Cu_{1.7}$ Clu/GAs make it a promising candidate for practical electrode applications in electrocatalytic CO_2RR for EtOH production.

Atomic coordination structure and chemical state analysis of $Cu_{1.7}$ Clu/GAs

Figure 3a illustrates the high-resolution Cu 2p XPS spectra of $Cu_{1.7}$ Clu/GAs and $Cu_{1.4}$ Clu/GAs. Two main peaks at 953.4 eV (Cu $2p_{1/2}$) and

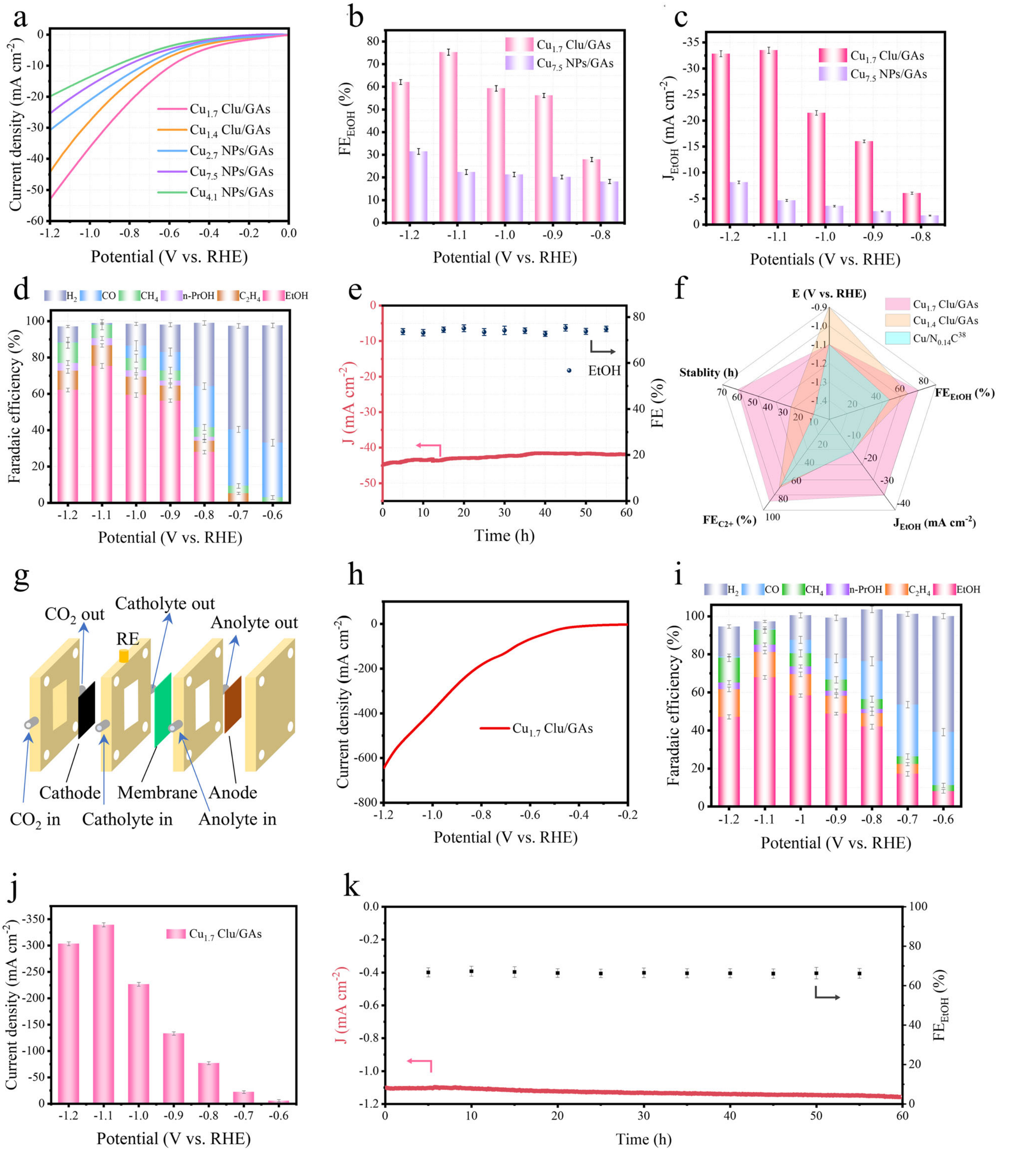

Fig. 2 | CO_2RR performance of $Cu_{1.7}$ Clu/GAs. **a** LSV curves of $Cu_{1.4}$ Clu/GAs, $Cu_{1.7}$ Clu/GAs, $Cu_{2.7}$ Clu/GAs, $Cu_{4.1}$ Clu/GAs, and $Cu_{7.5}$ Clu/GAs measured in CO_2 saturated electrolyte. **b** The FE of EtOH production detected by gas chromatography. **c** The partial current density of EtOH. **d** The FEs of all products on $Cu_{1.7}$ Clu/GAs at different potentials. **e** The long-term stability measurement of $Cu_{1.7}$ Clu/GAs at −1.1 V vs. RHE. **f** The comprehensive performance of $Cu_{1.7}$ Clu/GAs. **g** The schematic draw of the flow cell. **h** LSV curve of $Cu_{1.7}$ Clu/GAs in the flow cell. **i** The FEs of all products on $Cu_{1.7}$ Clu/GAs at different potentials (from −0.7 V to −1.2 V) in the flow cell. **j** The partial current densities of EtOH in the flow cell. **k** The long-term stability measurement results of $Cu_{1.7}$ Clu/GAs at −500 mA cm^{-2} in the flow cell. The potential was iR-corrected.

933.6 eV (Cu $2p_{3/2}$) were usually allocated to either Cu^0 or Cu^{+}[51] in $Cu_{1.7}$ Clu/GAs. C 1 s XPS spectrum of $Cu_{1.7}$ Clu/GAs and $Cu_{1.4}$ Clu/GAs present an additional peak at 282.9 eV corresponding to the Cu-C bond (Fig. 3b and Supplementary Fig. 21), which implies the effect of strong oxide-support interaction existed possibly between Cu_2O/CuO clusters and GAs[34,52–54]. According to the findings of organic element analysis tests (Supplementary Table 7), the oxygen content is highest in $Cu_{1.4}$ Clu/GAs, followed by $Cu_{1.7}$ Clu/GAs, and is lowest in GAs, consistent with the qualitative XPS results (Supplementary Figs. 21–23). This suggests that additional oxygen is introduced from the atmosphere during the

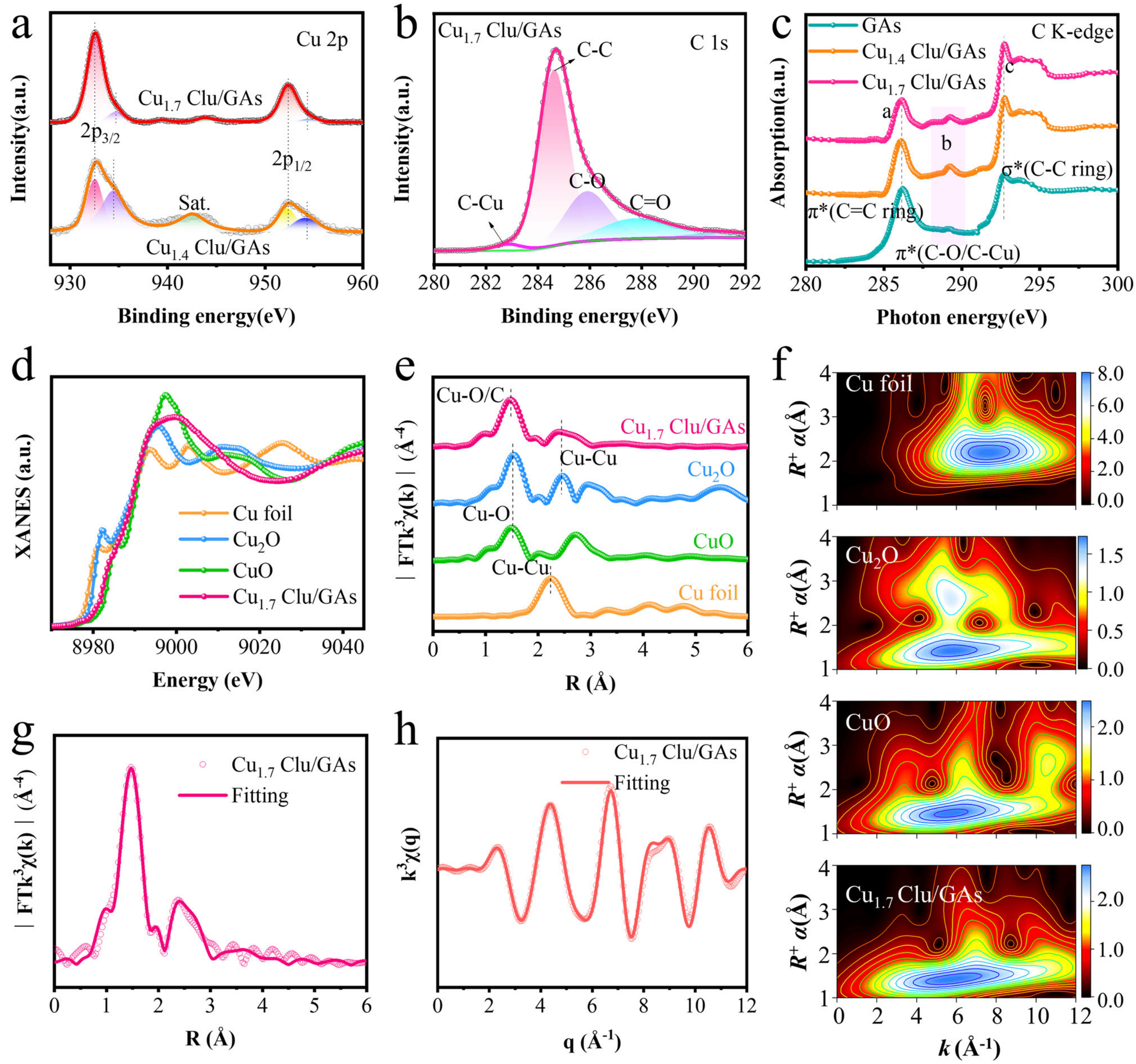

Fig. 3 | Atomic coordination structure and chemical state of $Cu_{1.7}$ Clu/GAs. **a** Cu 2p XPS spectra of $Cu_{1.7}$ Clu/GAs and Cu1.4 Clu/GAs. **b** The C 1 s XPS spectra of $Cu_{1.7}$ Clu/GAs. **c** Soft XAS of $Cu_{1.4}$ Clu/GAs, $Cu_{1.7}$ Clu/GAs and GAs. **d** The Cu K-edge XANES spectra of $Cu_{1.7}$ Clu/GAs and the references (Cu foil, Cu, CuO). **e** Cu K-edge FT k^3-weighted EXAFS spectra of $Cu_{1.7}$ Clu/GAs and references. **f** The WT-EXAFS profiles of $Cu_{1.7}$ Clu/GAs, Cu foil, Cu_2O, and CuO. **g** The EXAFS fitting result of $Cu_{1.7}$ Clu/GAs in the R space. **h** EXAFS fitting curve of $Cu_{1.7}$ Clu/GAs in q space.

pulsed discharge synthesis process of Cu Clu/GAs. X-ray diffraction (XRD) reveals a broad peak from the (002) of the GAs (Supplementary Fig. 24), the weak peaks of Cu were displayed in $Cu_{7.5}$ NPs/GAs. However, no diffraction peaks corresponding to Cu_2O crystals were detected in $Cu_{1.7}$ Clu/GAs, which indicates that the size of the Cu_2O clusters may be below the detection limit[55]. Raman spectroscopy was further employed to study the defect on GAs, two significant peaks at 1343 cm^{-1} and 1585 cm^{-1} represent the characteristics of graphene (Supplementary Fig. 25). The value of I_D/I_G increased to 1.19 from 1.09, indicating an increase in defects in graphene after the transient pulsed discharge. Combined with the analysis of XPS results, the formation of C-Cu bonds and the entry of oxygen atoms in the Cu Clu/GAs may be the main reasons for the increase of I_D/I_G. X-ray absorption spectroscopy (XAS) was utilized to further study the geometric and electronic structure of Cu Clu/GAs. The C K-edge absorption spectrum of GAs, $Cu_{1.7}$ Clu/GAs, and $Cu_{1.4}$ Clu/GAs under soft XAS were illustrated in Fig. 3c. The a, b, and c regions represent different types of chemical bonds, which are π*C = C (286.1 eV), σ*C-O/C-Cu (~ 289.2 eV), and π*C-C (292.7 eV). Furthermore, the σ*C-O/C-Cu of $Cu_{1.7}$ Clu/GAs and $Cu_{1.4}$ Clu/GAs were enhanced after pulsed discharge, which is consistent with the above results of XPS and Raman.

Figure 3d exhibits the Cu K-edge X-ray absorption near edge structure (XANES) spectra of the $Cu_{1.7}$ Clu/GAs and the references (Cu foil, CuO, and Cu_2O). The absorption edge of the $Cu_{1.7}$ Clu/GAs was between the CuO and Cu_2O, demonstrating the oxidation state of Cu is in the middle valence state (+1 to +2)[56,57]. A marginally higher rising edge could be attributed to the electron transfer from the GAs support to the Cu_2O nanocluster. The Fourier transformed (FT) k^3-weighted extended X-ray absorption fine structure (EXAFS) spectra of $Cu_{1.7}$ Clu/GAs (Fig. 3e) displayed an enhanced peak at 1.5 Å with a lower peak at 2.4 Å in R space. The enhanced peak came from the superimposed contribution of Cu-C and Cu-O, and the lower peak corresponding to the Cu-Cu bonds contribution revealed the existence of Cu_2O clusters in $Cu_{1.7}$ Clu/GAs. The Cu K-edge wavelet transform (WT) EXAFS results of $Cu_{1.7}$ Clu/GAs and references are presented in Fig. 3f. The high-intensity zone of the $Cu_{1.7}$ Clu/GAs in the first shell occupied a wider range than Cu foil, Cu_2O, CuO, which originated from the joint contribution of Cu-C, Cu-O, and Cu-Cu. Figure 3e, g, and Supplementary Fig. 26 depict the fitting results of $Cu_{1.7}$ Clu/GAs in R space, q space, and k space, respectively. The fitting result confirmed that the Cu-O/C bond length is 1.92 Å with the coordination number (CN) 3.2, and the Cu-Cu bond length is 2.55 Å with the CN 1.0 (Supplementary Table 8), indicating that Cu atoms in $Cu_{1.7}$ Clu/GAs were predominately coordinated with C/O atoms. Moreover, the EXAFS spectrum and fitting results in R space of $Cu_{1.4}$ Clu/GAs, $Cu_{2.7}$ NPs/GAs, $Cu_{4.1}$ NPs/GAs, and $Cu_{7.5}$ NPs/GAs are shown in Supplementary Fig. 27, the Cu-Cu bond was gradually strengthened with the increase in size. The fitting results in k space and q space are shown in Supplementary Fig. 28, and the WT EXAFS results are displayed in Supplementary Fig. 29. Notably, The CN of Cu-C/O was increased and the CN of Cu-Cu was decreased because the oxidation degree of Cu was weakened when the nanoparticle size increased from 1.4 nm to 7.5 nm, which is consistent with the results of HADDF-STEM.

Synthesis and structural characterizations of M Clu/GAs (M = Ni, Co, Pt, Ru)

The other metal clusters (M = Ni, Co, Pt, Ru) were easily generalized through the transient pulsed discharge synthesis strategy, only requiring the change of $CuCl_2$ to corresponding metal salts. Supplementary Figs. 30–33 present the HADDF-STEM images, XANES spectrum, FT-EXAFS, fitting, and WT EXAFS results of M Clu/GAs, they all exhibit uniform clusters on GAs with high quality. The best-fit structural parameters were shown in Supplementary Table 9, and the effect of strong metal/oxide with support existed on the M Clu/GAs. The extended investigations manifest the generality of the transient pulsed discharge strategy to construct unsymmetrical atomic structures and electronic structures for catalytic reactions. The electrochemical catalytic performance of four catalysts ($Co_{1.7}$ Clu/GAs, $Ni_{1.9}$ Clu/GAs, $Pt_{1.8}$ Clu/GAs, and $Ru_{1.7}$ Clu/GAs) for CO_2RR was tested in the H-type cell and the flow cell (Supplementary Figs. 34 and 35). The LSV curves of the four catalysts were utilized to evaluate their respective electrocatalytic performances. The FEs for different products of the four catalysts were obtained from 0 to −1.0 V vs. RHE, revealing distinct catalytic products. The primary electrochemical catalytic products for the $Co_{1.7}$ Clu/GAs catalyst were H_2, CO, HCOOH, and CH_4. For the $Ni_{1.9}$ Clu/GAs catalyst, the main products were H_2, CO, and HCOOH. The $Pt_{1.8}$ Clu/GAs catalyst primarily produced H_2 and CO, with a minor amount of CH_4 generated at −1.0 V vs. RHE. The $Ru_{1.7}$ Clu/GAs catalyst primarily yielded H_2, CO, and HCOOH, with a small quantity of CH_4 produced at −1.0 V vs. RHE. In comparison to Cu systems, GA-supported Co, Ni, Pt, and Ru clusters are unable to produce C_{2+} products during CO_2RR. Besides, the catalytic activity and selectivity for C_1 products require further improvement. These performances are influenced not only by the inherent properties of the metal elements themselves but also by factors such as the size, loading, and coordination structure of the metal nanoclusters.

In situ XAFS and in situ ATR-FTIR studies

Investigating the atomic structure-activity relationship of $Cu_{1.7}$ Clu/GAs on the CO_2RR process is essential to demonstrate the reaction mechanism. Therefore, in situ XAFS is employed to reveal the practical catalytic centers of $Cu_{1.7}$ Clu/GAs on the electrochemical catalytic CO_2RR (Supplementary Fig. 36). The in situ Cu K-edge XANES results of $Cu_{1.7}$ Clu/GAs at open circuit, −0.9 V, and −1.1 V vs. RHE are displayed in Fig. 4a. When the potential was changed, the sample underwent a drastic change. The energy at the absorption position gradually decreases as the potential decreases from 0 to −1.1 V (illustrated in Fig. 4a), while the intensity of the white line peak decreases, indicating an alteration in the valence state of Cu in $Cu_{1.7}$ Clu/GAs. The FT-EXAFS spectra of $Cu_{1.7}$ Clu/GAs in the CO_2RR process are presented in Fig. 4b. The peak position of Cu-Cu slightly transferred to the left, which revealed that the bond lengths of Cu-Cu were compressed a bit with the applied potential decreased. On the contrary, the Cu-O/C coordination bonds were in a stretched state during the CO_2RR process. In other words, the pinched Cu-Cu metal bonds provided mainly a large number of active sites for CO_2RR. The fitting results are shown in Supplementary Fig. 37 and Supplementary Table 10, the Cu-Cu bonds were enhanced and the Cu-C/O bonds were weakened gradually with the decrease of the operated potentials. Figure. 4c displays the WT-EXAFS results of $Cu_{1.7}$ Clu/GAs at open circuit, −0.9 V, and −1.1 V vs. RHE. The intensity maximum (~ 5.6 $Å^{-1}$) at open circuit and −0.9 V was similar to Cu_2O or CuO. With the decrease of the operated potential, a new intensity maximum (~ 10 $Å^{-1}$) was performed gradually, indicating that Cu_2O clusters were reduced on the GAs. Moreover, the high-intensity zone at ~5 $Å^{-1}$ was still maintained when the operated potential was −1.1 V, indicating that there was still a strong interaction between Cu clusters and graphene at the interface.

Furthermore, the normalized first derivative profiles of Cu K-edge XANES spectra with different potentials are shown in Supplementary Fig. 38. Furthermore, the oxidation state of Cu could be evaluated by comparing the peak position. The absorption edges were significantly changed with the decreased operated potential, which explicitly manifested that the process of CO_2RR on $Cu_{1.7}$ Clu/GAs is potential-dependent. When the absorption edge of Cu shifts to the lower energy, it is usually considered a reduced Cu valence state. The specific valence state of Cu under different conditions is depicted in Fig. 4d. The valence states of Cu in $Cu_{1.7}$ Clu/GAs were similar under ex-situ and open circuit conditions, and the valence state of Cu was between Cu^+ and Cu^{2+} due to the strong oxide-support effect. CO_2 was adsorbed at the active site of $Cu_{1.7}$ Clu/GAs in the CO_2-saturated electrolyte, resulting in the interaction between the 3*d* orbitals of the unpaired Cu atoms and the 2*p* orbitals of the carbon atoms in the CO_2. Upon the imposition of the reaction potential, a progressive decline in the oxidation state of Cu was observed. In the context of EXAFS analysis, it is important to note that the data obtained represents an average over the entire sample. At a potential of −1.1 V vs. RHE, the average oxidation state of Cu encompasses the collective contributions from Cu-Cu, Cu-support, and Cu-intermediates interaction on the $Cu_{1.7}$ Clu/GAs catalyst. As the active Cu sites on the surface of the Cu clusters adsorb the intermediates during the CO_2RR, this further leads to a redistribution of electrons at the asymmetric Cu-C/O active sites. Importantly, the electron modulation effect of the asymmetric Cu sites enhances their reactivity as the main adsorption sites.

To further study the important adsorbed intermediates in the CO_2RR process, the in situ ATR-FITR measurement was carried out at different operated potentials. Notably, distinct vibration peaks were detected at ~1450 cm^{-1} when the operated potentials reached −0.8 V vs. RHE (Fig. 4e), which could originate from the vibration of antisymmetric *CH_3, an important intermediate for C_{2+} products. Moreover, two new bands at around 1770 cm^{-1} and 1915 cm^{-1} can be identified as the C = O groups and the produced *CO bound to the Cu surface when the operating potential was below −0.8 V vs. RHE. This implies that the H* radical is affected by other products at −0.8 V vs. RHE, which is consistent with the electrochemical test findings. With the gradual decrease in applied potentials, the absorption peak of *CO peak was enhanced, indicating a strengthened interaction between the Cu sites and the *CO intermediates. Therefore, the in situ ATR-FTIR results provided experimental evidence elucidating the reaction mechanism for CO_2-to-EtOH conversion and demonstrated that *CH_3 and *CO are the important intermediate species adsorbed on the catalyst surface. Figure 4f provides the evolution process of the $Cu_{1.7}$ Clu/GAs catalyst

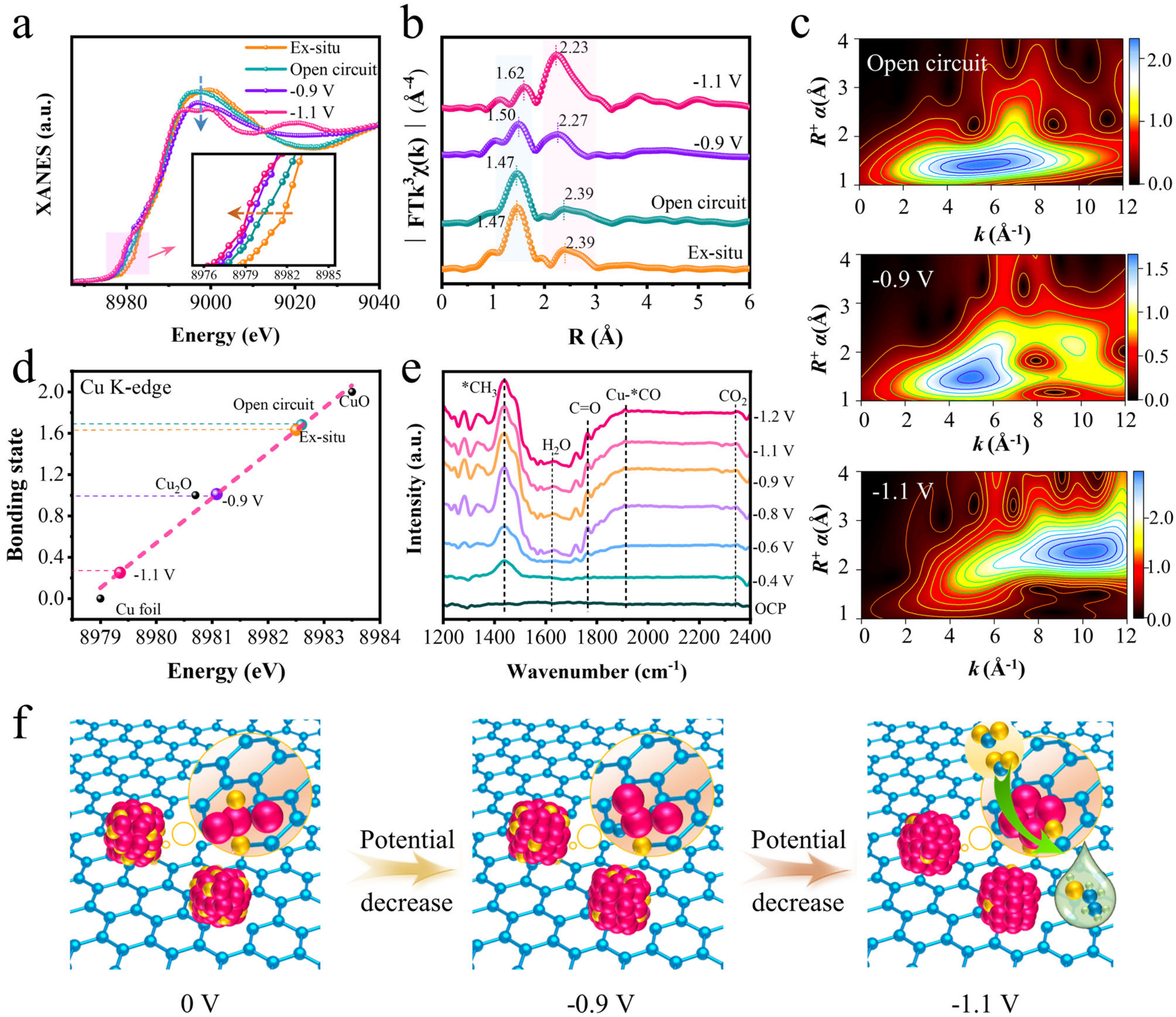

Fig. 4 | In situ XAFS and in situ ATR-FTIR characterizations of $Cu_{1.7}$ Clu/GAs. **a** The Cu K-edge XANES spectra of $Cu_{1.7}$ Clu/GAs at different potentials during the CO_2RR process. **b** The FT-EXAFS curves of $Cu_{1.7}$ Clu/GAs at ex-situ, open circuit, −0.9 V, and −1.1 V *vs.* RHE. **c** WT-EXAFS profiles of $Cu_{1.7}$ Clu/GAs at different potentials. **d** The calculated bonding state of Cu in $Cu_{1.7}$ Clu/GAs at different potentials and references. **e** In situ ATR-FTIR results of $Cu_{1.7}$ Clu/GAs at different potentials. **f** Proposed strategy for the process of electrocatalytic CO_2RR to produce ethanol on $Cu_{1.7}$ Clu/GAs at different potentials (yellow, O; blue, C; red, Cu).

at different potential conditions. The Cu_2O clusters were gradually reduced to Cu nanoclusters with the decrease of operated potential, and the Cu nanoclusters supported on r-GO exhibited good EtOH and C_{2+} production capabilities in electrochemical catalytic CO_2RR. After testing, Cu nanoclusters were gradually oxidized into Cu_2O clusters supported on r-GO due to their exposure to air.

In situ Raman, in situ NAP-XPS and DFT calculations

Bader charge and differential charge density analysis results displayed that the average partial charge of five Cu atoms in the Cu_4O-CuC_2O_1 moiety was +0.37 e^- due to the charge transfer between Cu and O-doped carbon substrates, specifically for the Cu atom bonding with oxygen atoms, as shown in Fig. 5a. This fractional charge state of Cu makes its oxidation state closed to 0.5 favoring C-C coupling, which is also a reliable descriptor for C_{2+} product selectivity, as evidenced by the previous report[58]. The moderate oxidation state of Cu (i.e., 0.5) induced by the partial oxygen coordination enhanced the C-C coupling to benefit the C_{2+} selectivity.

To further elucidate the reaction intermediates during the electrochemical CO_2RR, we performed in situ Raman spectroscopy (Supplementary Fig. 39) under a range of applied potentials (OCP, −0.8 V, −0.9 V, −1.0 V, −1.1 V vs. RHE). The peaks observed at 417 cm^{-1} and 600 cm^{-1} (Fig. 5b) are conventionally assigned to Cu-O vibrational modes[59,60], suggesting that despite the partial reduction of the Cu clusters at lower potentials, oxygen persists within the clusters. Moreover, oxygen within the Cu-C_2O_1 coordination with the support could also be discernible. The peaks at 593 cm^{-1} and 1160 cm^{-1} are indicative of *CO_2 stretching modes, reflecting the initial adsorption of CO_2 on the Cu sites. The peaks at 276 cm^{-1} and 352 cm^{-1} are indicative of Cu adsorbing the *CO species, a pivotal intermediate in the CO_2RR pathway towards ethanol formation. The Cu-*CO species at 352 cm^{-1} is typically regarded as being in a stretched configuration[61]. The peaks near 2025 cm^{-1} and 2100 cm^{-1} signify the low and high frequency bands of *C≡O stretching (Fig. 5c), respectively. An enhancement in peak intensity with increasingly negative applied potentials implies that reducing the potential augments the activity of the Cu sites, thereby facilitating increased adsorption of intermediates during the CO_2RR. The observed leftward shift of the Raman peaks as the potential decreases is ascribed to the electrochemical Stark effect[62,63].

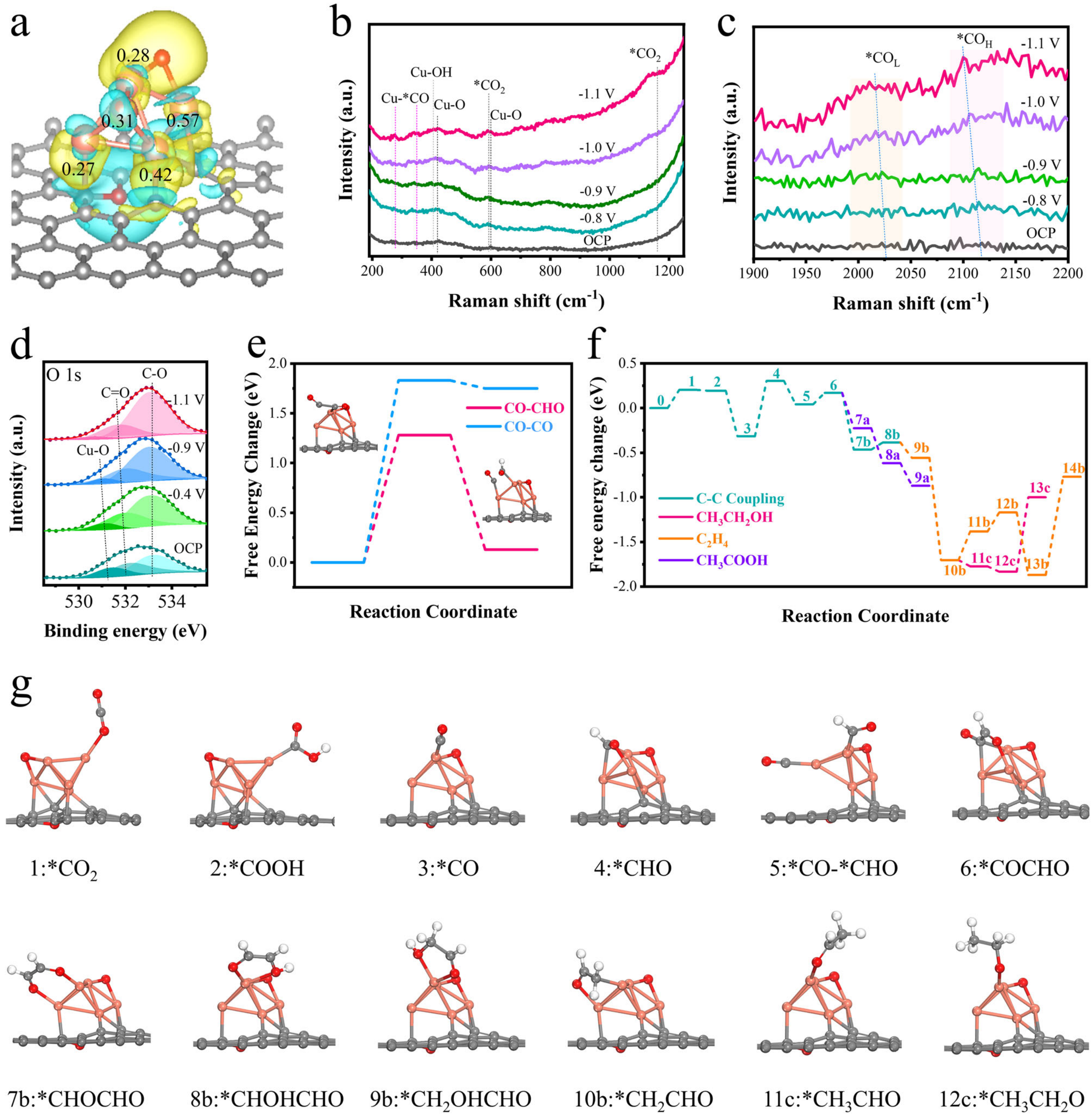

Fig. 5 | Theoretical CO_2RR activity of $Cu_{1.7}$ Clu/GAs. **a** Bader charge and differential charge density analysis results on the Cu_4O-CuC_2O_1 moiety. **b** In situ Raman spectra results of $Cu_{1.7}$ Clu/GAs during the electrocatalytic CO_2RR process (200-1250 cm^{-1}). **c** In situ Raman spectra results of $Cu_{1.7}$ Clu/GAs during the electrocatalytic CO_2RR process (1900–2200 cm^{-1}). **d** The spectra and peaks fitting of O 1s at different potentials in the NAP-XPS test. **e** The energy barrier of C-C coupling through CO-CO and CO-CHO dimerization, inset is the transition state. **f** Electrochemical CO_2 reduction pathway to CH_3CH_2OH, C_2H_4, CH_3COOH. **g** The optimized configurations of CH_3CH_2OH intermediates. Orange, red, white, and gray ball marks Cu, O, H, and C atoms, respectively.

In situ NAP-XPS tests were carried out to monitor the surface evolution of the $Cu_{1.7}$ Clu/GAs catalyst under varying potentials (OCP, −0.4 V, −0.9 V, −1.1 V vs. RHE) during the CO_2RR in the alkaline environment (Supplementary Fig. 40). Fitting of the O1s peaks at different potentials revealed a gradual weakening of the Cu-O bond as the potential decreased in Fig. 5d, indicating an increased degree of Cu reduction at lower potentials, consistent with the findings from in situ XAFS. The reduction in the Cu valence state is likely to influence the catalytic activity and selectivity. Concurrently, the ratio of the C-O bond peak area to the C = O bond peak area increased with decreasing operational potential, suggesting a higher prevalence of EtOH and n-PrOH products at −1.1 V. This observation is indicative of the catalyst's preference for C_{2+} product formation at more negative potentials, underscoring the potential-dependent selectivity of the CO_2RR on the $Cu_{1.7}$ Clu/GAs catalyst.

To gain a deeper understanding of the atomic-scale mechanism underlying the CO_2 reduction process leading to C_2 products (ethanol, ethylene, and acetic acid) on the asymmetric Cu_4O-CuC_2O_1 moiety, we undertook a meticulous study of the hydrogenation process, accounting for the potential involvement of various intermediates through DFT calculations (Supplementary data 1). Supplementary Fig. 41 elucidates the relative stability of various doped carbon substrates considering the Cu atom with different coordinated numbers of C and O atoms (such as CuC_3, CuC_2O_1, CuC_1O_2, and CuO_3) by the calculations of formation energies, indicating that doped carbon substrate with CuC_2O_1 moiety possesses lowest formation energy of all. Supplementary Fig. 42 marks the optimized Cu_4O-CuC_2O_1 configurations, where the Cu_4O cluster is bonded to the CuC_2O_1-graphene, with numerals "0-3" designating the prospective adsorption sites of the Cu_4O cluster. Supplementary Fig. 43 illustrates the possibly adsorbed models of the CO_2 molecule, in which the Cu "2" site in a quasi-linear configuration exhibits a stable structure with an adsorption free energy of 0.20 eV. Supplementary Figs. 44 and 45 present the optimized models of the *COOH and *CO species, respectively, with adsorption free energies of 0.19 eV and −0.32 eV. Note that the calculations of adsorption free energies of intermediates for CO_2RR on the Cu_4O-CuC_2O_1 catalyst were benchmarked with the energy of CO_2, H_2, and H_2O molecules. Hence CO species owned much stronger binding strength on the Cu_4O-CuC_2O_1 surface with lower adsorption energy than that of pure Cu surface, such as Cu(111), and Cu(100)[64–66], significantly enhancing the surface coverage of *CO species. Based on the previous reports[2,67], in combination with experimental characterization results in Figs. 4e and 5b, the *CO intermediate served as a pivotal species for the formation of the C_2 product, which can be obtained from the C-C coupling process via *CO dimerization, *CO-*CHO, or *CO-*COH binding step. After detailed DFT simulations in Supplementary Fig. 46, the *CHO species on the Cu_4O-CuC_2O_1 moiety exhibits a much lower adsorption energy of 0.30 eV than that of *COH with 1.27 eV, revealing the preferential generation of the *CHO species in the hydrogenation process of *CO intermediate to support *CO-*CHO coupling, not prone to *CO-*COH coupling.

Figure 5e shows the minimum energy pathway of C-C coupling through the *CO-*CO and *CO-*CHO process, corresponding optimized configurations on the initial state (IS), transition state (TS), and final state (FS) in Supplementary Figs. 47 and 48. The *CO-*CHO coupling process exhibits a smaller reaction energy and activation energy barrier with 0.13 and 1.28 eV than that of *CO-*CO dimerization with 1.75 and 1.83 eV, respectively, indicating C-C coupling preferred by *CO-*CHO linking step. Besides, the reaction energy and activation barrier of the CO-CHO coupling process on the Cu_4O-CuC_2O_1 catalyst is also lower than that of Cu (100) by 0.44 and 1.36 eV, and Cu (111) surface by 0.35 and 1.44 eV in Supplementary Figs. 49–51, respectively, signifying enhanced C-C coupling activity by the introduction of asymmetrical Cu clusters. Because of the exclusion of explicit solvent, pH, electrode potential, and the intermediate coverage effects, both C-C coupling processes all possess a little higher energy barriers, specifically for the *CO-*CO coupling, compared with the previous work on the bulk Cu (111) and Cu (100) surfaces[65,67,68]. Based on the above analysis, all the primary steps of C_2 products before C-C coupling are the same, i.e., $CO_2 \rightarrow {}^*CO_2 \rightarrow {}^*COOH \rightarrow {}^*CO \rightarrow {}^*CHO \rightarrow {}^*CO\text{-}{}^*CHO \rightarrow {}^*CO{}^*CHO$. Due to the lower activation barrier, all the intermediates after C-C coupling are investigated based on the *COCHO species. The lowest energy pathways towards the identified CH_3CH_2OH, C_2H_4, and CH_3COOH products were illustrated in Fig. 5f, and the optimized models of intermediates were displayed in Fig. 5g, Supplementary Figs. 52 and 53. The detection of key reaction intermediates (such as $^*CH_3$ and *CO) above in situ Raman and in situ FTIR experiments supports the theoretical calculations. The CH_3COOH path ramified at the sixth proton-coupled-electron transfer (PCET) step, while the CH_3CH_2OH and C_2H_4 pathway shared the former ten PCETs, and bifurcated at the 11^{th} coupled proton-electron-transfer process. The common intermediate for the CH_3CH_2OH and C_2H_4, such as *HCO-CHO (7b), was superior to form than the intermediates of CH_3COOH (7a: $COCH_2O$) by lower adsorption energy of −0.24 eV, indicating the preferential generation of CH_3CH_2OH and C_2H_4 before CH_3COOH[64,69,70]. This mechanistic investigation verified the experimental measurements in Fig. 2d, where CH_3CH_2OH and C_2H_4 are the major products, with no detection of CH_3COOH species. Compared to the CH_3CH_2OH and C_2H_4 formation from CO_2 (which are all the 12-electron reduction products), the common intermediate for CH_3CH_2OH, i.e., CH_3CHO (11c) has much lower adsorption energy than C_2H_4 intermediate (11b: CH_2CH_2O) by 0.33 eV. Additionally, free energy diagram analysis further unearthed that the potential-determined step (PDS) of CH_3CH_2OH formation was the last step (12c → 13c: $^*CH_3CH_2O \rightarrow CH_3CH_2OH$) with the free energy change of 0.83 eV, much lower than that of C_2H_4 with 1.10 eV (PDS: 13b → 14b: $^*OH \rightarrow {}^* + H_2O$), revealing the preferred generation of C_2 product CH_3CH_2OH. This agrees with the much higher percentage of CH_3CH_2OH over the C_2H_4 product in the experimental results for the Cu_4O-CuC_2O_1 catalyst as shown in Fig. 2d.

Discussion

In summary, we successfully achieved precise control over the cluster size of unsymmetrical Cu Clu/GAs catalysts through a pulsed discharge strategy. By adjusting the charging voltage from 7.4 kV to 9.0 kV, we synthesized a range of Cu Clu/GAs with varying cluster sizes (1.4 nm, 1.7 nm, 2.7 nm, 4.1 nm, 7.5 nm). Among these, $Cu_{1.7}$ Clu/GAs, characterized by unsymmetrical Cu_4O-CuC_2O_1 moieties on GAs, demonstrated superior catalytic activity and stability for CO_2 reduction to EtOH and C_{2+} products at a charging voltage of 8.6 kV. Our experimental results, supported by theoretical calculations, reveal that the enhanced electrochemical performance is attributed to the optimal atomic and electronic structures of the Cu_4O-CuC_2O_1 moieties, establishing an interesting structure-activity relationship. The pulsed discharge strategy utilized in this study presents a promising approach for the scalable production of Cu Clu/GAs catalysts. The ability to finely tune cluster sizes and their associated catalytic properties indicates that this method could be applied in industrial contexts, particularly in established CO_2 reduction systems aimed at sustainable ethanol production. The high efficiency of these catalysts in converting CO_2 to ethanol and C_{2+} products underscores their potential to contribute to carbon neutrality efforts. The insights gained from this study not only advance our understanding of catalyst design and performance but also lay a solid foundation for the rational development of next-generation catalysts tailored for specific industrial applications. Overall, this work significantly enhances the feasibility of sustainable CO_2 utilization, thereby supporting the global transition towards carbon neutrality.

Methods

Chemicals

Copper chloride ($CuCl_2$, 99%, Alfa Aesar), Cobalt chloride ($CoCl_2$, 99%, Alfa Aesar), Nickel chloride ($NiCl_2$, 99%, Alfa Aesar), Hydrogen hexachloroplatinate ($H_2PtCl_4 \cdot xH_2O$, 99.995%, Alfa Aesar), Ruthenium chloride ($RuCl_3$, 99%, Alfa Aesar), methanol (analytical grade, Alfa Aesar), $KHCO_3$ (Sigma Aldrich), Nafion D-521 dispersion (5 wt%, Alfa Aesar).

Preparation of Cu Clu/GAs

In a typical synthesis, the single-layer graphene oxide (GO) was diluted and mixed fully in deionized water ($GO/H_2O = 2$ mg/g). The uniformly dispersed GO was put into a hydrothermal reactor, heated at 180 °C for 6 h, and graphene hydrogel gradually formed. The graphene hydrogel was fully immersed in $CuCl_2$ aqueous solution for 5 h, and then quickly frozen in liquid nitrogen. Subsequently, GA support $CuCl_2$ nanocrystals ($CuCl_2$/GA) were formed by freeze-drying. Afterward, the as-prepared $CuCl_2$/GA was filled into the copper discharge tube for the pulsed discharge process. Then the discharge tube containing $CuCl_2$/GA was connected to the discharge circuit. The discharge voltage could be changed to produce different size metal clusters/nanoparticles supported by GAs. When the air switch is triggered, the intense pulsed current passes through the copper discharge tube and $CuCl_2$/GA. The pulsed current and voltage features of $Cu_{1.7}$ Clu/GAs and other samples are displayed in Supplementary Table 1.

The CO_2RR tests are presented in Supplementary Note. 2, the XAFS measurements and data processing are depicted in Supplementary Notes. 3-5. The in situ ATR-FTIR, in situ Raman, and in situ NAP-XPS tests and the details of DFT calculation methods are shown in Supplementary Notes. 6-9.

^{1}H Nuclear magnetic resonance analysis

The yield of liquid products, such as EtOH, and n-PrOH during constant potential electrolysis (4000 s) was quantified by nuclear magnetic resonance (NMR) spectroscopy[15]. These products were recorded on a Bruker Avance III NMR spectrometer operating at 11.7 T (500 MHz ^{1}H), and dimethyl sulfoxide (DMSO, 99.9%) was utilized as an internal standard. The same spectral acquisition parameters were used for all spectra to ensure full relaxation and quantification. The acquisition parameters were: time domain data size (65536); number of dummy scans (2); number of scans (16); spectral width (19.9899 ppm); loop count time domain (1); spectral width in Hertz (10,000 Hz); filter width (125,000 Hz); pause width (45°); delay 1 (5 s) and delay 2 (0 s). For the NMR tests, a 700 μl electrolyte sample was mixed with 35 μl of internal standard solution (the mixture of 10.0 μl DMSO and 14 ml of D_2O). The ratio of relative peak area obtained standard curves of each product.

ECSA measurement

The ECSA is measured by cycling the electrode under the same conditions used for catalytic testing within the non-Faradaic region. When the electrode is cycled at varying scan rates (v), the variation in non-Faradaic current density (j) should exhibit a linear relationship with the scan rate, allowing the slope to provide the double-layer capacitance (C_{dl}=j/v). The density of electrochemically active sites can be calculated by multiplying the active site density of a flat surface by the roughness factor (R_f). Similarly, the specific surface area of the electrode can be estimated by multiplying the geometric surface area by the roughness factor. We conducted cyclic voltammetry (CV) to supplement the measurements of the double-layer capacitance values for $Cu_{1.7}$ Clu/GAs and $Cu_{1.4}$ Clu/GAs to calculate the ECSA of the catalysts. The calculation is defined as follows: ECSA=R_fS, where S represents the actual surface area of a smooth metal electrode, typically equivalent to the geometric area of the carbon paper electrode (in this work, S = 1.0 cm^2). The roughness factor R_f is estimated through the ratio of the double-layer capacitance C_{dl} of the working electrode to that of the corresponding smooth metal electrode (C_{dlref}). Here, we use the average value of 0.04 mF cm^{-2} for C_{dlref} in alkaline solutions without taking the used material and measurement conditions into account[71]. The C_{dl} values are determined by measuring the capacitive current associated with double-layer charging, utilizing the scan rate dependence of cyclic voltammetry. The potential window for the cyclic voltammetry was set between 0.05 V and 0.35 V (vs. RHE) in a saturated CO_2 environment with 0.5 M $KHCO_3$ solution. The scan rates employed were 10, 20, 40, 60, 80, 100, and 120 mV s^{-1}.

Reporting summary

Further information on research design is available in the Nature Portfolio Reporting Summary linked to this article.

Data availability

The data supporting the findings of this study are available within the article and its Supplementary Information files. All other relevant source data are available from the corresponding authors. Source data are provided with this paper.

References

1. Lees, E. W. et al. Gas diffusion electrodes and membranes for CO_2 reduction electrolysers. *Nat. Rev. Mater.* **7**, 55–64 (2022).
2. Zheng, Y. et al. Understanding the roadmap for electrochemical reduction of CO_2 to multi-carbon oxygenates and hydrocarbons on copper-based catalysts. *J. Am. Chem. Soc.* **141**, 7646–7659 (2019).
3. Birdja, Y. Y. et al. Advances and challenges in understanding the electrocatalytic conversion of carbon dioxide to fuels. *Nat. Energy* **4**, 732–745 (2019).
4. Shen, H. et al. Acidic CO_2-to-EtOH electrolysis with industrial-level current on phase engineered tin sulfide. *Nat. Commun.* **14**, 2843 (2023).
5. Jiang, B. et al. Boosting EtOH Production in Electrocatalytic CO_2 Reduction over Wide Potential Window on Pd Surfaces. *J. Am. Chem. Soc.* **140**, 2880–2889 (2018).
6. Qiao, Y. et al. Engineering the Local Microenvironment over Bi Nanosheets for Highly Selective Electrocatalytic Conversion of CO_2 to EtOH in Strong Acid. *ACS Catal* **12**, 2357–2364 (2022).
7. Liu, W. et al. Unraveling the interfacial effect of PdBi bimetallic catalysts on promoting CO_2 electroreduction to EtOH. *Nano Res.* **16**, 10822–10831 (2023).
8. Zouaoui, N. et al. Electroreduction of CO_2 to EtOH on amine modified Pb electrodes. *J. Mater. Chem. A.* **7**, 11272–11281 (2019).
9. Guo, C. et al. Electrocatalytic Reduction of CO_2 to Ethanol at Close to Theoretical Potential via Engineering Abundant Electron-Donating $Cu^{\delta+}$ Species. *Angew. Chem. Int. Ed.* **61**, e202205909 (2022).
10. Wei, B. et al. Efficient electrocatalytic reduction of CO_2 to EtOH by bimetallic In-Cu nanoparticles with controlled growth facet. *Appl. Catal. B* **283**, 119646 (2021).
11. Koh, J. H. et al. Facile CO_2 Electro-Reduction to EtOH via Oxygen Bidentate Intermediate Stabilized by High-Index Planes of Bi Dendrite Catalyst. *ACS Catal* **7**, 5071–5077 (2017).
12. Reller, C. et al. Selective electroreduction of CO_2 toward ethylene on nano dendritic copper catalysts at high current density. *Adv. Energy Mater.* **7**, 1602114 (2017).
13. Liu, K. et al. The atomic interface effect of single atom catalysts for electrochemical hydrogen peroxide production. *Nano Res.* **16**, 10724–10741 (2023).
14. Wang, Y. et al. Reticular chemistry in electrochemical carbon dioxide reduction. *Sci. China Mater.* **63**, 1113–1141 (2020).
15. Pan, C. et al. Neighboring sp-hybridized carbon participated molecular oxygen activation on the interface of sub-nanocluster CuO/graphdiyne. *J. Am. Chem. Soc.* **144**, 4942–4951 (2022).
16. Wang, P. et al. Boosting electrocatalytic CO_2-to-ethanol production via asymmetric C-C coupling. *Nat. Commun.* **13**, 3754 (2022).
17. Da, Y. et al. The applications of single-atom alloys in electrocatalysis: progress and challenges. *Smart Mat.* **4**, e1136 (2023).
18. Kim, C. et al. Cu/Cu_2O Interconnected Porous Aerogel Catalyst for Highly Productive Electrosynthesis of Ethanol from CO_2. *Adv. Funct. Mater.* **31**, 2102142 (2021).
19. Deng, Z. W. et al. Rational design and energy catalytic application of high-loading single-atom catalysts. *Rare Met* **43**, 4844–4866 (2024).
20. Zang, Y. et al. Selective CO_2 electroreduction to ethanol over a carbon-coated CuO_x catalyst. *Angew. Chem. Int. Ed* **134**, e202209629 (2022).
21. Wang, Q. et al. Recent advances in copper-based catalysts for electrocatalytic CO_2 reduction toward multi-carbon products. *Nano Research Energy* **3**, e9120112 (2024).
22. Luo, M. et al. Hydroxide promotes carbon dioxide electroreduction to ethanol on copper via tuning of adsorbed hydrogen. *Nat. Commun.* **10**, 5814 (2019).
23. Xu, H. et al. Highly selective electrocatalytic CO_2 reduction to ethanol by metallic clusters dynamically formed from atomically dispersed copper. *Nat. Energy* **5**, 623–632 (2020).
24. Xia, W. et al. Adjacent Copper Single Atoms Promote C-C Coupling in Electrochemical CO_2 Reduction for the Efficient Conversion of Ethanol. *J. Am. Chem. Soc.* **145**, 17253–17264 (2023).

25. Ding, J. et al. A tin-based tandem electrocatalyst for CO_2 reduction to ethanol with 80% selectivity. *Nat. Energy* **8**, 1386–1394 (2023).
26. Zhang, C. C. et al. Enhanced hydrogen evolution performance by 3D ordered macroporous Ru-CoP@NC electrocatalysts. *Rare Met.* **43**, 1095–1107 (2024).
27. Liu, Z. et al. Switching CO_2 Electroreduction toward Ethanol by Delocalization State-Tuned Bond Cleavage. *J. Am. Chem. Soc.* **146**, 14260–14266 (2024).
28. Wang, Y. et al. Enhanced Local CO Coverage on Cu Quantum Dots for Boosting Electrocatalytic CO_2 Reduction to Ethylene. *Adv. Funct. Mater.* 2417764 (2024).
29. Yang, S. et al. *In Situ* Structure Refactoring of Bismuth Nanoflowers for Highly Selective Electrochemical Reduction of CO_2 to EtOH. *Adv. Funct. Mater.* 2301984 (2023).
30. Zhang, P. et al. Inter-site structural heterogeneity induction of single atom Fe catalysts for robust oxygen reduction. *Nat. Commun.* **15**, 2062 (2024).
31. Li, Y. et al. Boosted hydrogen evolution kinetics of heteroatom-doped carbons with isolated Zn as an accelerant. *PNAS* **121**, e2315362121 (2024).
32. Wu, Q. et al. Atomically precise copper nanoclusters for highly efficient electroreduction of CO_2 towards hydrocarbons via breaking the coordination symmetry of Cu site. *Angew. Chem. Int. Ed.* **135**, e202306822 (2023).
33. Zhang, A. et al. Harmonizing the electronic structures of the adsorbate and catalysts for efficient CO_2 reduction. *Nano Lett.* **19**, 6547–6553 (2019).
34. Rong, W. et al. Size-Dependent Activity and Selectivity of Atomic-Level Copper Nanoclusters during CO/CO_2 Electroreduction. *Angew. Chem. Int. Ed.* **60**, 466–472 (2021).
35. Shen, J. & Wang, D. How to select heterogeneous CO_2 reduction electrocatalyst. *Nano Res. Energy* **3**, e9120096 (2024).
36. Yu, J. et al. Electronic Oxide–Support Strong Interactions in the Graphdiyne-Supported Cuprous Oxide Nanocluster Catalyst. *J. Am. Chem. Soc.* **145**, 1803–1810 (2023).
37. Jia, Z. et al. Fully-exposed Pt-Fe cluster for efficient preferential oxidation of CO towards hydrogen purification. *Nat. Commun.* **13**, 6798 (2022).
38. Hu, Q. et al. Facile synthesis of sub-nanometric copper clusters by double confinement enables selective reduction of carbon dioxide to methane. *Angew. Chem. Int. Ed.* **59**, 19054–19059 (2020).
39. Li, J. et al. Promoting CO_2 Electroreduction to Hydrocarbon Products via Sulfur-Enhanced Proton Feeding in Atomically Precise Thiolate-Protected Cu Clusters. *Angew. Chem. Int. Ed.* **63**, e202412144 (2024).
40. Gu, Z. et al. Efficient electrocatalytic CO_2 reduction to C_{2+} alcohols at defect-site-rich Cu surface. *Joule* **5**, 429–440 (2021).
41. Zheng, T. et al. Copper-catalysed exclusive CO_2 to pure EtOH conversion via single atom alloying. *Nat. Nanotechnol.* **16**, 1386–1393 (2021).
42. Su, X. et al. Complementary *Operando* Spectroscopy identification of in-situ generated metastable charge-asymmetry Cu_2-CuN_3 clusters for CO_2 reduction to ethanol. *Nat. Commun.* **13**, 1322 (2022).
43. Luna, P. D. et al. Catalyst electro-redeposition controls morphology and oxidation state for selective carbon dioxide reduction. *Nat. Catal.* **1**, 103–110 (2018).
44. Xu, F. et al. Oxygen-Bridged Cu Binuclear Sites for Efficient Electrocatalytic CO_2 Reduction to Ethanol at Ultralow Overpotential. *J. Am. Chem. Soc.* **146**, 9365–9374 (2023).
45. Zhan, C. et al. Key intermediates and Cu active sites for CO_2 electroreduction to ethylene and ethanol. *Nat. Energy* **9**, 1485–1496 (2024).
46. Bingqing, W. et al. Low-dimensional material supported single-atom catalysts for electrochemical CO_2 reduction. *SmartMat* **3**, 84–110 (2022).
47. Wu, Z. et al. Engineering bismuth-tin interface in bimetallic aerogel with a 3D porous structure for highly selective electrocatalytic CO_2 reduction to EtOH. *Angew. Chem. Int. Ed.* **60**, 12554–12559 (2021).
48. Liu, S. et al. Efficient Electrochemical Reduction of CO_2 to EtOH over Sub-2nm SnO_2 Quantum Wires with Exposed Grain Boundaries. *Angew. Chem. Int. Ed.* **58**, 8499–8503 (2019).
49. Liu, K. et al. Ultra-Fast Pulsed Discharge Preparation of Coordinatively Unsaturated Asymmetric Copper Single-Atom Catalysts for CO_2 Reduction. *Adv. Funct. Mater.* **34**, 2312589 (2024).
50. Sarkisov, G. S., Hamilton, A. & Sotnikov, V. I. Inverse polarity effect for electrical explosion of fine metal wires in vacuum. *Phys. Rev. E* **98**, 053203 (2018).
51. Chen, P. et al. Interfacial engineering of cobalt sulfide/graphene hybrids for highly efficient ammonia electrosynthesis. *PNAS* **116**, 6635–6640 (2019).
52. Jia, Y. et al. Electronic Oxide-Support Strong Interactions in the Graphdiyne Supported Cuprous Oxide Nanocluster Catalyst. *J. Am. Chem. Soc.* **145**, 1803–1810 (2023).
53. Cai, Y. et al. Insights on forming N, O-coordinated Cu single-atom catalysts for electrochemical reduction CO_2 to methane. *Nat. Commun.* **12**, 586 (2021).
54. Shang, H. et al. Engineering unsymmetrically coordinated Cu-S_1N_3 single atom sites with enhanced oxygen reduction activity. *Nat. Commun.* **11**, 3049 (2020).
55. Tang, C. et al. Tailoring acidic oxygen reduction selectivity on single-atom catalysts via modification of first and second coordination spheres. *J. Am. Chem. Soc.* **143**, 7819–7827 (2021).
56. Cai, R. et al. Engineering Cu (I)/Cu (0) interfaces for efficient ethanol production from CO_2 electroreduction. *Chem* **10**, 211–233 (2024).
57. Yang, Y. et al. Operando studies reveal active Cu nanograins for CO_2 electroreduction. *Nature* **614**, 262–269 (2023).
58. Haobo, L. et al. C_{2+} Selectivity for CO_2 Electroreduction on Oxidized Cu-Based Catalysts. *J. Am. Chem. Soc.* **145**, 14335–14344 (2023).
59. Yaran, Z. et al. Speciation of Cu Surfaces During the Electrochemical CO Reduction Reaction. *J. Am. Chem. Soc.* **142**, 9735–9743 (2020).
60. Chao, Z. et al. Revealing the CO Coverage-Driven C-C Coupling Mechanism for Electrochemical CO_2 Reduction on Cu_2O Nanocubes via Operando Raman Spectroscopy. *ACS Catal.* **11**, 7694–7701 (2021).
61. Jiapeng, J. et al. Steering the Reaction Pathway of CO_2 Electroreduction by Tuning the Coordination Number of Copper Catalysts. *J. Am. Chem. Soc.* **146**, 15917–15925 (2024).
62. Junyuan, D. et al. Active and conductive layer stacked superlattices for highly selective CO_2 electroreduction. *Nat. Commun.* **13**, 2039 (2022).
63. Rongming, C. et al. Engineering Cu(I)/Cu(0) interfaces for efficient ethanol production from CO_2 electroreduction. *Chemistry* **10**, 211–233 (2024).
64. Du, C. et al. Cascade electrocatalysis via AgCu single-atom alloy and Ag nanoparticles in CO_2 electroreduction toward multicarbon products. *Nat. Commun.* **14**, 6142 (2023).
65. Santatiwongchai, J., Faungnawakij, K. & Hirunsit, P. Comprehensive mechanism of CO_2 electroreduction toward ethylene and ethanol: the solvent effect from explicit water-Cu (100) interface models. *ACS Catal.* **11**, 9688–9701 (2021).
66. Cheng, T., Xiao, H. & Goddard, I. I. I. W. A. Full atomistic reaction mechanism with kinetics for CO reduction on Cu (100) from ab initio molecular dynamics free-energy calculations at 298 K. *PNAS* **114**, 1795–1800 (2017).
67. Todorova, T. K., Schreiber, M. W. & Fontecave, M. Mechanistic understanding of CO_2 reduction reaction (CO_2RR) toward multi-carbon products by heterogeneous copper-based catalysts. *ACS Catal.* **10**, 1754–1768 (2019).

68. Garza, A. J., Bell, A. T. & Head-Gordon, M. Mechanism of CO_2 reduction at copper surfaces: pathways to C_2 products. *ACS Catal.* **8**, 1490–1499 (2018).
69. Shenghua, C. et al. PO_4^{3-} MOFEncapsulating N-Heterocyclic Carbene-Ligated Copper Single-Atom Site Catalysttowards Efficient Methane Electrosynthesis. *Angew. Chem. Int. Ed.* **134**, e202114450 (2022).
70. Wang, X. et al. Efficient electrically powered CO_2-to-ethanol via suppression of deoxygenation. *Nat. Energy* **5**, 478–486 (2020).
71. Du, Y. et al. Continuous strain tuning of oxygen evolution catalysts with anisotropic thermal expansion. *Nat. Commun.* **15**, 1780 (2024).

Acknowledgements

This work was supported by National Natural Science Foundation of China (Grant No. 12372332 to X.G., 12002048 to X.G. and 22375019 to W.C.), the Beijing Natural Science Foundation (Grant No. 2212018 to X.G.), Beijing Institute of Technology Research Fund Program for Young Scholars (Grant No. 2022CX01011 to W.C. and Grant No. XSQD-202002004 to X.G.), and the Beijing Institute of Technology Research and Innovation Promoting Project (Grant No. 2022YCXZ003 to K.L.). The Start-up Foundation for Senior Talents of Jiangsu University (21JDG041 to Z.S. (Zhongti Sun)), and the China Postdoctoral Science Foundation (2023M731357 to Z.S. (Zhongti Sun)). We thank the theoretical calculations performed on the Northwest District of the Sugon National Supercomputer Center and the A6 Zone of the Beijing Super Cloud Computing Center, supported by PARATERA.

Author contributions

X.G., W.C. and P.C. conceived the idea, designed the research and wrote the paper. K.L. carried out the sample synthesis, characterization and wrote the paper. Z.S. (Zhiyi Sun) performed CO_2RR measurements. W.C. carried out the in situ synchrotron radiation XAFS measurements and data analysis. Q.Z. revised this paper. H.S., G.L. and Z.S. (Zhongti Sun) performed the DFT calculations and processed the data. All the authors discussed the results and commented on the manuscript.

Competing interests

The authors declare no competing interests.

Additional information

Supplementary information The online version contains supplementary material available at https://doi.org/10.1038/s41467-025-56534-1.

Correspondence and requests for materials should be addressed to Zhongti Sun, Wenxing Chen, Xin Gao or Pengwan Chen.

Peer review information *Nature Communications* thanks Jaeyoung Lee, and the other, anonymous, reviewer(s) for their contribution to the peer review of this work. A peer review file is available.